A Surface Cauchy-Born model for silicon nanostructures

Harold S. Park [a,*], Patrick A. Klein [b]

[a] *Department of Mechanical Engineering, University of Colorado, Boulder, CO 80309, USA*
[b] *Franklin Templeton Investments, San Mateo, CA 94403, USA*

Abstract

We present a Surface Cauchy-Born approach to modeling non-centrosymmetric, semiconducting nanostructures such as silicon that exist in a diamond cubic lattice structure. The model is based on an extension to the standard Cauchy-Born theory in which a surface energy term that is obtained from the underlying crystal structure and governing interatomic potential is used to augment the bulk energy. The incorporation of the surface energy leads naturally to the existence of surface stresses, which are key to capturing the size-dependent mechanical behavior and properties of nanomaterials. We present the approach in detail, then demonstrate its capabilities by calculating the minimum energy configurations of silicon nanowires due to surface stresses as compared to full scale atomistic calculations.
© 2008 Elsevier B.V. All rights reserved.

1. Introduction

Nanowires have been studied intensely in recent years due to their unique and often superior mechanical, electrical and optical properties that arise because of their nanometer size scale [1–3]. Because of these unique properties, nanowires will be utilized as structural materials, bio-sensors, force and mass detectors, as circuitry and interconnects in future nanoscale devices, and as the basic building blocks of nanoelectromechanical systems (NEMS) [4–7]. The recent trend towards miniaturizing microelectromechanical systems (MEMS) into NEMS stems from the fact that NEMS are generally lighter and stiffer, which leads to increased sensitivity to forces, masses and environmental variations while concurrently operating at higher vibrational frequencies.

Silicon has, for various reasons, emerged as the material of choice for future NEMS. The major reason is that silicon is already the fundamental material used in the microelectronics industry [8]; with the scaling down in size of

microelectronics components to the nanoscale, existing silicon fabrication technology will be used to build smaller and smaller silicon-based devices. Furthermore, silicon is also a key optoelectronic material [9], which further enhances the utility of silicon-based NEMS. The overall impact of silicon can be judged by noting that the majority of currently devised NEMS utilize silicon or silicon-based compounds as their basic building block [6,10,11].

NEMS are fundamentally different from MEMS because nanoscale free surfaces play a dominant role in determining the elastic properties of nanowires [1–3]. One particularly important effect due to nanoscale free surfaces is surface stresses [12–16]. Surface stresses on nanomaterials arise due to an imbalance in the forces acting on surface atoms due to their lack of bonding neighbors. Because surface atoms have a different bonding environment than atoms that lie within the material bulk, the elastic properties of surfaces differ from those of the bulk material, and the effects of the difference between surface and bulk elastic properties on the effective elastic properties of the nanowire become magnified with decreasing structural size/increasing surface area to volume ratio. Such size-dependence of mechanical properties has been observed in both semiconducting [17–24] and metallic [25–33] nanowires.

---

* Corresponding author. Tel.: +1 303 492 7750.
 E-mail address: harold.park@colorado.edu (H.S. Park).

The importance of nanoscale surface effects on nanomaterials has led to three distinct approaches to modeling their mechanical behavior and properties. The first has been through classical molecular dynamics (MD) simulations. Unfortunately, MD simulations are generally intractable at the length scales (>50 nm) at which nanowire-based NEMS are currently synthesized experimentally. For example, a cube that is 100 nm on a side would contain nearly 60 million gold atoms, which would not only require prohibitively expensive parallel MD calculations, but would also generate enormous amounts of redundant and unnecessary data. Therefore, while MD simulations have been beneficial for elucidating size effects on the mechanical behavior and properties of ultrasmall (<10 nm) nanowires [31,29,32, 23,33,34], scaling these results to larger nanowires while accounting for variations in size, surface effects and geometry at time scales larger than nanoseconds [35] has not been achieved due to computational expense.

Alternatively, a variety of enhanced continuum models that strive to capture the non-bulk elastic behavior of nanomaterials have been proposed [36,12,37–39,30,40–49]. In general, due to assumptions utilized to make the analyses tractable, the coupled effects of geometry, surface area to volume ratio and system size on the mechanical properties of nanowires have not been quantified, nor have surface stress effects arising directly from atomistic principles been included in the models, which are generally in two-dimensions. Furthermore, the complex nature of the analytic models has in general precluded the possibility of using them in finite element (FE) calculations to analyze the size-dependent behavior of metal nanowires.

The final approach to modeling the mechanics of nanomaterials has been the recent explosion in multiscale computational methods, which attempt to combine the insights into the detailed response of materials that are available through atomistics with the reduced computational expense that continuum approaches offer [50–64]. However, these approaches generally neglect atomic-scale surface stresses due to the fact that ghost, or pad atoms are necessary at the atomistic/continuum boundary to ensure energy and force continuity; this precludes the possibility of utilizing them to analyze and design nanowire-based NEMS devices.

To model surface effects on nanomaterials, Park and co-workers recently developed the Surface Cauchy-Born (SCB) model to capture surface stress effects on FCC metal nanostructures within a continuum mechanics framework [65–67]. The SCB extends the traditional bulk Cauchy-Born (BCB) theory [68–70,50] by augmenting the continuum bulk energy density with a surface energy density that enables it to capture nanoscale surface stress effects. The SCB model is advantageous as it enables the solution of three-dimensional nanomechanical boundary value problems including surface stress effects using traditional nonlinear finite element (FE) methods; this makes it computationally tractable, particularly for large systems, that direct atomistic simulations cannot model. In addition, many of the well-

developed advantages of FE calculations, including automated meshing for arbitrary geometries, nonlinear solution methodologies and ease and choice of boundary condition imposition are directly applicable for the solution of nanomechanical boundary value problems using the SCB model. The SCB model [65] has been used to analyze surface stress effects on the minimum energy configurations [66] and the resonant frequencies [67] of metal nanowires, as well as nanoscale resonant mass sensing [71] and surface-stress-driven thermoelastic dissipation [72].

In the present work, we develop the SCB model for diamond cubic (DC) lattice structures, which opens the door to studying the size-dependent mechanical behavior of semiconducting nanomaterials such as silicon. The theoretical foundations for studying DC lattices including treatment of internal degrees of freedom originated with Stakgold [69] and Weiner [70], and was extended by Tadmor et al. [73] who developed a BCB model for the Stillinger–Weber potential while a BCB model for DC lattice structures interacting via the Tersoff potential [74,75] was recently developed by Aluru and co-workers [76,77]. The relative paucity of BCB research on DC lattices and thus semiconducting materials is due to the fact that unlike FCC crystals, the DC lattice is not centrosymmetric, which leads to a unit cell that must include more than a single atom.

We develop the SCB model for silicon assuming a ⟨100⟩ axial orientation with {100} transverse surfaces. While silicon {100} surfaces are well-known to exhibit various types of dimerizations and reconstructions [78,79], we will consider only the ideal {100} surfaces in this work, while leaving the reconstructed surfaces for future research. Numerical simulations on silicon nanowires demonstrate the applicability of the approach for modeling silicon nanostructures through comparison with fully atomistic calculations for silicon using the Tersoff potential [75].

2. Diamond cubic lattices

2.1. Atomistic description

Silicon is well-known to occur naturally in the DC lattice structure, which is formed through two interpenetrating FCC lattices, where the two FCC lattices are offset by a factor of $(a_0/4, a_0/4, a_0/4)$, with a_0 being the lattice parameter. The DC lattice is illustrated in Fig. 1, which illustrates the interpenetrating FCC lattices.

In the present work, we utilize the T3 form of the Tersoff potential [75] and the resulting parameters, which are summarized in Table 1. The T3 is named as such due to the fact that two earlier versions of the Tersoff potential suffered from various shortcomings, including not predicting diamond as the ground state of silicon, inaccuracies in the bulk elastic constants [74], and inaccurate modeling of the {100} surfaces of silicon [78]. The T3 form of the Tersoff potential can be written as
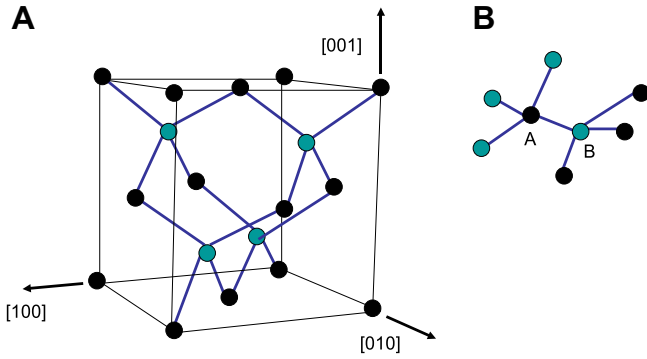
Fig. 1. Illustration of the diamond cubic lattice structure of silicon. Black atoms represent standard FCC unit cell atoms, while green atoms represent the interpenetrating FCC lattice. The drawn bonds connect atoms in FCC lattice B to atoms in FCC lattice A.

$$U = \frac{1}{2} \sum_{i \neq j} V_{ij}, \quad V_{ij} = f_C(r_{ij})(f_R(r_{ij}) + b_{ij} f_A(r_{ij})), \quad (1)$$

where r_{ij} is the distance between atoms i and j, f_C is a cut-off function, which is used to ensure that the Tersoff potential is effectively a nearest neighbor potential, f_R is a repulsive function, f_A is an attractive function, and b_{ij} is the bond order function, which is used to modify the bond strength depending on the surrounding environment. The various functions all have analytic forms, which are given as

$$f_R(r_{ij}) = A e^{-\lambda r_{ij}}, \quad (2)$$

$$f_A(r_{ij}) = -B e^{-\mu r_{ij}}, \quad (3)$$

$$b_{ij} = \left(1 + \beta^n \zeta_{ij}^n\right)^{-1/2n}, \quad (4)$$

where

$$\zeta_{ij} = \sum_{k \neq i,j} f_C(r_{ik}) g(\theta_{ijk}) \quad (5)$$

and

$$g(\theta_{ijk}) = 1 + \frac{c^2}{d^2} - \frac{c^2}{d^2 + (h - \cos\theta_{ijk})^2}. \quad (6)$$

The bond order function (4) is the part of the potential that incorporates many-body effects through the θ_{ijk} term in Eqs. (5) and (6). Thus, for each bond $i - j$, the bond order term b_{ij} depends on the number of neighboring atoms $j - k$ that fall within a certain cutoff radius R_C from atom i (see Table 1).

Because the Tersoff potential and the DC lattice will figure prominently into the resulting BCB and SCB formulations, we discuss additional relevant points at this juncture. The Tersoff potential was designed as a nearest neighbor potential, due to the computational expense involved in evaluating the bond order function b_{ij} for many atomic pairs. For a bulk atom, this implies that it will have exactly four nearest neighbors in the undeformed or initial configuration, with the undeformed nearest neighbor bond distances being equal to $\sqrt{3}a_0/4$ as mentioned above. Thus,

Table 1
Tersoff T3 potential parameters [75]

Parameter	Value
A	1830.8 eV
B	471.18 eV
λ	2.4799 Å^{-1}
μ	1.7322 Å^{-1}
β	1.1 $\times 10^{-6}$
c	100390
d	16.217
h	−0.59825
n	0.78734
R_C	2.70 Å

the energetics of a representative bulk atom can be reproduced using a five-atom unit cell, following that as introduced by Tang et al. [76], where the center atom A in Fig. 1B represents the first FCC bravais lattice, and the surrounding four atoms B represent the atoms on the second FCC bravais lattice.

The fact that the DC lattice is comprised of two interpenetrating FCC lattices has important implications for formulating a BCB model. The first is that the DC lattice structure is not centrosymmetric, which means that the unit cell must contain more than a single atom, and leads to additional computational expense in modeling the larger unit cell. The second important fact is that the two interpenetrating FCC lattices must be able to translate rigidly with respect to each other, necessitating the introduction of an internal degree of freedom Ξ for each unit cell. The internal degree of freedom Ξ is associated with atom A in Fig. 1B, indicating that it can translate rigidly with respect to the B atoms in the second bravais lattice. This internal degree of freedom Ξ serves an identical purpose as the shift vector that has been introduced in the CB modeling of carbon nanotubes [80,81].

2.2. Bulk Cauchy-Born overview

The BCB model is based on Green elastic theory, in which continuum stress and modulus are derived assuming the existence of a strain energy density function Φ. In order to satisfy material frame indifference, the strain energy density Φ must be expressed as a function of the right stretch tensor $\mathbf{C}$, i.e. $\Phi(\mathbf{C})$, where $\mathbf{C} = \mathbf{F}^T\mathbf{F}$ and $\mathbf{F}$ is the continuum deformation gradient.

The BCB and SCB models are finite deformation constitutive models that explicitly represent the stretching and rotation of bonds undergoing large deformation through continuum mechanics-based kinematic quantities such as the deformation gradient $\mathbf{F}$, or the stretch tensor $\mathbf{C} = \mathbf{F}^T\mathbf{F}$ [82]. Under deformations which can be represented as homogeneous over the unit cell scale, the approximation exactly reproduces the response of the corresponding, fully atomistic response representation of the crystal.

To create a link between atomistics and continua, the strain energy density can be constructed for crystalline

materials by considering the bonds in a representative volume of the crystal [50,83]. In general, the strain energy density for a centrosymmetric crystal interacting via pair interactions is defined in terms of the interatomic potential U as [83]

$$\Phi(\mathbf{C}) = \frac{1}{\Omega_0} \sum_{i=1}^{n_b} U(r^{(i)}(\mathbf{C})). \tag{7}$$

In (7), n_b is the total number of bonds to a representative bulk atom, Ω_0^a is the representative atomic volume in the undeformed configuration and $r^{(i)}$ is the deformed bond length, which follows the relationship:

$$r^{(i)} = \sqrt{\mathbf{R}_0^{(i)} \cdot \mathbf{C} \mathbf{R}_0^{(i)}}, \tag{8}$$

where $\mathbf{R}_0$ is the undeformed bond vector. From the strain energy density given in (7), one can obtain standard continuum stress measures such as the second Piola–Kirchoff (PK2) stress ($\mathbf{S}$) and the spatial tangent modulus ($\mathscr{C}$) as

$$\mathbf{S}(\mathbf{C}) = 2\frac{\partial \Phi(\mathbf{C})}{\partial \mathbf{C}} = \frac{1}{\Omega_0^a} \sum_{i=1}^{n_b} \left(U'(r^{(i)}) \frac{\partial r^{(i)}}{\partial \mathbf{C}} \right), \tag{9}$$

$$\mathscr{C} = 2\frac{\partial \mathbf{S}(\mathbf{C})}{\partial \mathbf{C}}. \tag{10}$$

The strain energy density (7) is exact in describing the change in energy per volume of a bulk atom in a corresponding defect-free atomistic system subject to homogeneous deformation. Furthermore, the continuum stress measure in (9) is derived using atomistic information; thus the BCB hypothesis is said to be hierarchically multiscale in nature. We note that the BCB model can also be utilized in conjunction with various interatomic interactions such as embedded atom (EAM) potentials [84,50,66] for FCC metals, Tersoff-type potentials for silicon [73,76], or Brenner-type potentials for carbon nanotubes [81,80].

There are two major assumptions underlying the BCB hypothesis. The first is that, as mentioned above, the underlying atomistic system is constrained to deform homogeneously according to the stretch tensor $\mathbf{C}$. This restriction can be relaxed, for example through development of the non-local CB model [50], if the consideration of lattice defects is important. The second major assumption is that all points at which the BCB hypothesis is applied are assumed to lie in the bulk because $\Phi(\mathbf{C})$ does not account for surface effects. Therefore, in order to capture nanoscale free surface effects such as surface stresses, we will augment the bulk energy density in (7) with a surface energy density which accounts for the non-bulk potential energy that atoms lying along the surfaces of a body exhibit.

2.3. Bulk unit cell

Upon having introduced the Tersoff potential and BCB preliminaries, we are now in a position to define the bulk and surface unit cells and the resulting stress and modulus measures that will be required for the finite element solution of the governing equilibrium equations. The current formulation is similar to that given in Tang et al. [76], with modifications to correctly introduce the internal degree of freedom in a manner that ensures frame indifference.

Converting the Tersoff potential energy (1) into a strain energy density Φ to account for a five atom unit cell, we write, following Tang et al. [76]:

$$\Phi(r_{1j}) = \frac{1}{2\Omega_0} \sum_{j=2}^{5} V_{1j}(r_{1j}), \tag{11}$$

where $i = 1$ in (11) because atom i is considered the center of the unit cell (see Fig. 1), and the summation goes over the four nearest neighbor bonds $j = 2, 3, 4, 5$. The full expression for the strain energy density $\Phi(r_{1j})$ can be written as

$$\Phi(r_{1j}) = \frac{V_{1j}}{2\Omega_0} = A\mathrm{e}^{-\lambda r_{1j}} - B\mathrm{e}^{-\mu r_{1j}} \left(1 + \beta^n \left(\sum_{k \neq i,j} g(\theta_{1jk}) \right)^n \right)^{-1/2n}, \tag{12}$$

where again the multibody effects of the bonding environment are captured through the $g(\theta_{1jk})$ term. The strain energy density in (12) can be turned into an object that is useful for BCB modeling by making the bond lengths r_{1j} functions of the continuum deformation quantities and the internal degree of freedom as

$$r_{1j} = |\mathbf{r}_{1j}| = |\mathbf{F}(\mathbf{R}_{1j} + \mathbf{\Xi})|, \quad j = 2, 3, 4, 5, \tag{13}$$

where $\mathbf{r}_{1j}$ is the deformed bond vector and $\mathbf{R}_{1j}$ is the undeformed bond vector between atoms 1 and j and $\mathbf{\Xi}$ is the shift introduced between the two interpenetrating FCC lattices in the undeformed configuration. The incorporation of the internal degrees of freedom and writing the bond lengths in terms of $\mathbf{F}$ results in a modified strain energy density function as

$$\Phi(\mathbf{C}) = \widetilde{\Phi}(\mathbf{C}, \mathbf{\Xi}(\mathbf{C})). \tag{14}$$

Using (9), we can calculate the PK2 stress as

$$\frac{1}{2}\mathbf{S} = \frac{\partial \Phi}{\partial \mathbf{C}} = \frac{\partial \widetilde{\Phi}}{\partial \mathbf{C}} + \frac{\partial \widetilde{\Phi}}{\partial \mathbf{\Xi}} \frac{\partial \mathbf{\Xi}}{\partial \mathbf{C}}. \tag{15}$$

To keep the crystal at an energy minimum, the internal degrees of freedom are constrained to deform according to $\mathbf{\Xi}^*$, which leads to the following relationship:

$$\frac{\partial \widetilde{\Phi}}{\partial \mathbf{\Xi}^*} = 0, \tag{16}$$

which reduces the expression for the second Piola–Kirchoff stress in (15) to

$$\mathbf{S} = 2\frac{\partial \widetilde{\Phi}}{\partial \mathbf{C}}. \tag{17}$$

For a given state of deformation, the internal degrees of freedom $\mathbf{\Xi}$ can be determined using an iterative procedure

$$\mathbf{\Xi}^{(i+1)} = \mathbf{\Xi}^{(i)} + \Delta\mathbf{\Xi}^{(i+1)}, \tag{18}$$

where the initial guess for the degrees of freedom is $\boldsymbol{\Xi}^{(0)} = \mathbf{0}$, meaning that all atoms begin from the position enforced by the homogeneous deformation of the CB rule; the superscripts indicate iteration numbers. The update for the internal degrees of freedom can then be written as, using Newton's method

$$\Delta\boldsymbol{\Xi}^{(i+1)} = -\left(\frac{\partial^2\widetilde{\Phi}^{(i)}}{\partial\boldsymbol{\Xi}\partial\boldsymbol{\Xi}}\right)^{-1}\frac{\partial\widetilde{\Phi}^{(i)}}{\partial\boldsymbol{\Xi}}. \tag{19}$$

In order to calculate the modulus, we use (10) to write

$$\begin{aligned}
\frac{1}{4}\mathscr{C}_{\mathrm{IJKL}} &= \frac{\partial^2\Phi}{\partial\mathscr{C}_{\mathrm{KL}}\partial\mathscr{C}_{\mathrm{IJ}}} \\
&= \frac{\partial^2\widetilde{\Phi}}{\partial\mathscr{C}_{\mathrm{KL}}\partial\mathscr{C}_{\mathrm{IJ}}} + \frac{\partial^2\widetilde{\Phi}}{\partial E_q\partial\mathscr{C}_{\mathrm{IJ}}}\frac{\partial E_q}{\partial\mathscr{C}_{\mathrm{KL}}} + \frac{\partial\widetilde{\Phi}}{\partial E_p}\frac{\partial^2 E_p}{\partial\mathscr{C}_{\mathrm{KL}}\partial\mathscr{C}_{\mathrm{IJ}}} \\
&\quad + \left(\frac{\partial^2\widetilde{\Phi}}{\partial\mathscr{C}_{\mathrm{KL}}\partial E_p} + \frac{\partial^2\widetilde{\Phi}}{\partial E_q\partial E_p}\frac{\partial E_q}{\partial\mathscr{C}_{\mathrm{KL}}}\right)\frac{\partial E_p}{\partial\mathscr{C}_{\mathrm{IJ}}}..
\end{aligned} \tag{20}$$

Eq. (20) can be simplified by the knowledge that $\frac{\partial\boldsymbol{\Xi}}{\partial\mathbf{C}}$ needs to be evaluated for the equilibrium preserving motion $\boldsymbol{\Xi}^*$, which leads to the expression

$$\frac{\partial^2\widetilde{\Phi}}{\partial\mathscr{C}_{\mathrm{KL}}\partial E_p^*} + \frac{\partial^2\widetilde{\Phi}}{\partial E_q^*\partial E_p^*}\frac{\partial E_q^*}{\partial\mathscr{C}_{\mathrm{KL}}} = 0. \tag{21}$$

Solving (21) gives

$$\frac{\partial E_q^*}{\partial\mathscr{C}_{\mathrm{KL}}} = -\left(\frac{\partial^2\widetilde{\Phi}}{\partial E_q^*\partial E_p^*}\right)^{-1}\frac{\partial^2\widetilde{\Phi}}{\partial\mathscr{C}_{\mathrm{KL}}\partial E_p^*}. \tag{22}$$

Using (22), the spatial tangent modulus can be expressed as

$$\mathscr{C}_{\mathrm{IJKL}} = M_{\mathrm{IJKL}} - A_{\mathrm{IJp}}A_{\mathrm{KLq}}(\mathbf{D}^{-1})_{pq}, \tag{23}$$

where

$$\begin{aligned}
M_{\mathrm{IJKL}} &= 4\frac{\partial^2\widetilde{\Phi}}{\partial\mathscr{C}_{\mathrm{IJ}}\partial\mathscr{C}_{\mathrm{KL}}}, \\
D_{pq} &= \frac{\partial^2\widetilde{\Phi}}{\partial E_p^*\partial E_q^*}, \\
A_{\mathrm{IJp}} &= 2\frac{\partial^2\widetilde{\Phi}}{\partial\mathscr{C}_{\mathrm{IJ}}\partial E_p^*}.
\end{aligned} \tag{24}$$

The elastic constants were calculated, and were found to be, in Mbars

$$\begin{aligned}
C_{11} &= 1.426, \\
C_{12} &= 0.754, \\
C_{44}^0 &= 1.188, \\
C_{44} &= 0.690,
\end{aligned} \tag{25}$$

where C_{44}^0 is the value of C_{44} if internal relaxation due to $\boldsymbol{\Xi}$ is not allowed. We note that these values match those obtained by Tersoff [85] in fitting the T3 parameters to experiment, and also indicate that ignoring the internal degree of freedom $\boldsymbol{\Xi}$ leads to predictions of the shear elastic constant

C_{44} that are overly stiff, as would be expected for an over-constrained system.

3. Surface Cauchy-Born model for silicon

The theoretical basis for the SCB model was developed in earlier works [65–67] for FCC crystals; in this work, we extend the idea to account for surface stresses in DC crystals. The theoretical difficulty that is overcome in this work is that the DC lattice is not centrosymmetric as FCC lattices are. Therefore, unlike previous work using the SCB model for FCC metals, a single atom unit cell for the surface atoms cannot be utilized, and instead a larger surface unit cell was developed in this work for DC crystals.

We consider in this work the unreconstructed, or ideal {100} surfaces of silicon. While it is known that the {100} surfaces of silicon undergo various reconstructions [78,79], we consider the ideal {100} surface as a benchmark to investigate the ability of the SCB model to capture surface effects on diamond cubic lattice structures.

To develop an SCB model for silicon, there are two major differences from the BCB model described earlier in this work [50,76], and in earlier research which developed the SCB model for FCC lattices [65,66]. First, the strain energy is normalized by a measure of *area* Γ_0 instead of volume Ω_0, leading to a surface energy density $\gamma(\mathbf{C})$. This is done because the total energy of a nanostructure can be written as

$$\sum_{\alpha=1}^{n_{\mathrm{atoms}}} U_\alpha(r) \approx \int_{\Omega_0^{\mathrm{bulk}}} \Phi(\mathbf{C})\,\mathrm{d}\Omega + \int_{\Gamma_0} \gamma(\mathbf{C})\,\mathrm{d}\Gamma, \tag{26}$$

where $U_\alpha(r)$ represents the potential energy for each atom α. As discussed earlier, because surface atoms have a different bonding environment than atoms that lie within the material bulk, the elastic properties of surfaces differ from those of the bulk material, and the effects of the difference between surface and bulk elastic properties on the effective elastic properties of the nanostructure become magnified with decreasing structural size/increasing surface area to volume ratio.

It should be noted that in the absence of deformation, the bulk energy density $\Phi(\mathbf{C})$ in (26) equals the cohesive energy of silicon (4.63 eV) divided by the representative volume Ω_0 of a bulk atom. The surface energy density $\gamma(\mathbf{C})$ in (26) has a similar meaning; it is simply the energy of the surface atom (or surface unit cell, in the case of the present work) divided by the representative area Γ_0 of a surface atom. Besides the volume or area normalizing factor, the surface energy density $\gamma(\mathbf{C})$ differs from the bulk energy density $\Phi(\mathbf{C})$ only due to the fewer number of bonds that surface atoms have as compared to bulk atoms.

The relative importance of surface area to volume ratio can be quantified by calculating the ratio for various length scales. For a cube with volume 1 m^3, the surface area to volume ratio is 6×10^{-10} Å^{-1}. For a cube with a volume of 1 μm^3, the surface area to volume ratio increases to

6×10^{-4} Å^{-1}. However, for a cube with a volume of 1 nm^3, the surface area to volume ratio is 0.6 Å^{-1}. Thus, it is apparent that the different elastic properties of surfaces will make an increasingly important contribution to the effective elastic properties of materials with characteristic lengths in the nanometer regime.

Second, the unit cell for the surfaces is different from that of the bulk due to the lack of bonding neighbors for atoms lying at or near a surface. For FCC crystals previously investigated using the SCB model [65–67], the surface unit cell was comprised of multiple single atom unit cells, with a different unit cell single atom unit cell for each layer of undercoordinated atoms away from the surface. However, because the diamond cubic lattice is not centrosymmetric, using multiple single atom unit cells for each different undercoordinated layer of surface and near surface atoms is not possible. Furthermore, the surface unit cell has additional complications due to the incorporation of the internal degrees of freedom $\mathbf{\Xi}^s$, which must also be accounted for.

Fig. 2 shows the nine atom surface unit cell that we utilize to develop the modified SCB model for unreconstructed {100} silicon surfaces. The rationale for the nine atom unit cell is as follows. Atom 1 has bonds to just two atoms, instead of four, because it lies on a surface; these bonds are to atoms 2 and 6, which lie one layer into the bulk. Note that atoms 2 and 6 both effectively behave as bulk atoms, as they have a full complement of four nearest neighbors. In analyzing Fig. 2, it seems apparent that the black atoms (atoms 1, 5 and 7 on the surface, and atoms 3, 4, 8, 9 two layers into the bulk) represent a distinct FCC lattice A that should be able to translate with respect to atoms 2 and 6, which are part of the interpenetrating FCC lattice B. Therefore, we assign an internal degree of freedom $\mathbf{\Xi}^s$, where the superscript s designates an internal surface degree of freedom, to all the black atoms (1, 3, 4, 7, 8, 9) of FCC lattice A in Fig. 2. We note that because the approach requires the crystal surface geometry,
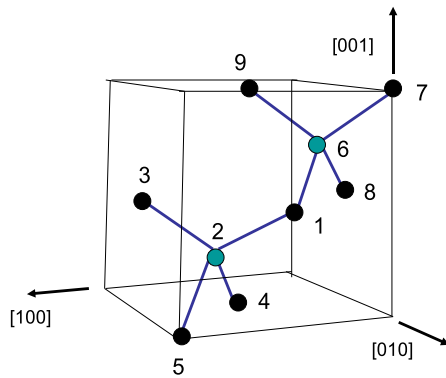
the formulation changes if the surface geometry is altered, for example if the {100} surface dimerizes in the 2×1 reconstruction.

The resulting strain energy density γ for the surface unit cell seen in Fig. 2 can thus be written as

$$\gamma = \frac{1}{\Gamma_0} \left(\sum_{j=2,6} V_{1j}(r_{1j}) + \sum_{k=1,7,8,9} V_{6k}(r_{6k}) + \sum_{m=1,3,4,5} V_{2m}(r_{2m}) \right),$$
(27)

where Γ_0 is the area per atom on the surface. Following (13), we express the bond lengths for the surface unit cell as:

$$\begin{aligned} r_{1j} &= |\mathbf{r}_{1j}| = |\mathbf{F}(\mathbf{R}_{1j} + \mathbf{\Xi}^s)|, \quad j = 2, 6, \\ r_{6k} &= |\mathbf{r}_{6k}| = |\mathbf{F}(\mathbf{R}_{6k} + \mathbf{\Xi}^s)|, \quad k = 1, 7, 8, 9, \\ r_{2m} &= |\mathbf{r}_{2m}| = |\mathbf{F}(\mathbf{R}_{2m} + \mathbf{\Xi}^s)|, \quad m = 1, 3, 4, 5. \end{aligned}$$
(28)

Incorporating the bond lengths that have been modified by the deformation gradient $\mathbf{F}$ and the internal degrees of freedom $\mathbf{\Xi}^s$ in (28) creates a modified surface energy density $\tilde{\gamma}(\mathbf{C})$ from (27), where the surface energy density has been modified analogously to the procedure outlined previously for the bulk energy density in (15) and (16) to enforce the energy minimizing condition

$$\frac{\partial \tilde{\gamma}}{\partial \widetilde{\mathbf{\Xi}}^s} = 0,$$
(29)

where $\widetilde{\mathbf{\Xi}}^s$, similar to the meaning in the bulk case in (16), represents the deformation of the surface internal degrees of freedom necessary to minimize the surface energy. Using the modified surface energy density $\tilde{\gamma}(\mathbf{C})$, we arrive at the expression for the surface PK2 stress $\mathbf{S}^s(\mathbf{C})$, where the superscript s here and below indicates surface values

$$\mathbf{S}^s(\mathbf{C}) = 2 \frac{\partial \tilde{\gamma}(\mathbf{C})}{\partial \mathbf{C}}.$$
(30)

We call the stress in (30) a surface stress because it is not a stress in the traditional sense, i.e. the normalization factor is an area, instead of a volume. Therefore, the units of the surface stress are force/length, as opposed to the force/area units typically found for bulk stresses. In addition, the surface stresses $\mathbf{S}^s(\mathbf{C})$ are 3×3 tensors with normal components which allow surface relaxation due to undercoordinated atoms lying at material surfaces [65,66].

Similarly, the surface tangent modulus can be written as

$$\mathscr{C}_{IJKL}^s = M_{IJKL}^s - A_{IJp}^s A_{KLq}^s (\mathbf{D}^{-1})_{pq}^s,$$
(31)

where

$$\begin{aligned} M_{IJKL}^s &= 4 \frac{\partial^2 \tilde{\gamma}}{\partial \mathscr{C}_{IJ}^s \partial \mathscr{C}_{KL}^s}, \\ D_{pq}^s &= \frac{\partial^2 \tilde{\gamma}}{\partial \widetilde{\mathbf{\Xi}}_p^s \partial \widetilde{\mathbf{\Xi}}_q^s}, \\ A_{IJp}^s &= 2 \frac{\partial^2 \tilde{\gamma}}{\partial \mathscr{C}_{IJ}^s \partial \widetilde{\mathbf{\Xi}}_p^s}. \end{aligned}$$
(32)

Fig. 2. Illustration of the nine atom surface unit cell for the surface with a [010] normal of a diamond cubic crystal. Black atoms represent FCC lattice A, while green atoms represent the interpenetrating FCC lattice B. The drawn bonds connect atoms in FCC lattice B to atoms in FCC lattice A.

4. Finite element formulation

Having defined the surface energy densities $\tilde{\gamma}(\mathbf{C})$ for the surface unit cell, we can immediately write the total potential energy Π of the system including external loads $\mathbf{T}$ as

$$\Pi(\mathbf{u}) = \int_{\Omega_0^{bulk}} \widetilde{\Phi}(\mathbf{C})\mathrm{d}\Omega + \int_{\Gamma_0} \tilde{\gamma}_{\Gamma_0}(\mathbf{C})\mathrm{d}\Gamma - \int_{\Gamma_0} (\mathbf{T} \cdot \mathbf{u})\mathrm{d}\Gamma. \tag{33}$$

In order to obtain a form suitable for FE calculations, we introduce the standard discretization of the displacement field $\mathbf{u}(\mathbf{X})$ using FE shape functions as

$$\mathbf{u}(\mathbf{X}) = \sum_{I=1}^{nn} N_I(\mathbf{X})\mathbf{u}_I, \tag{34}$$

where N_I are the shape or interpolation functions, nn are the total number of nodes in the discretized continuum, and $\mathbf{u}_I$ are the displacements of node I [82,86]. Substituting (27), (11) and (34) into (33) and differentiating gives the minimizer of the potential energy and also the FE nodal force balance [82]
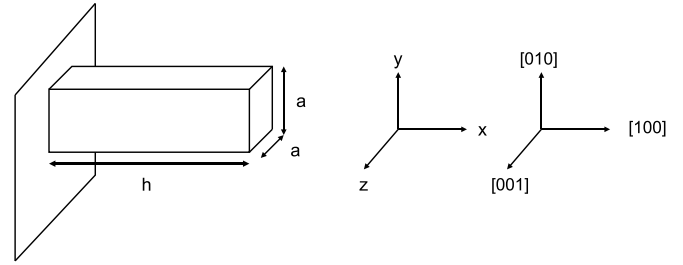

Fig. 3. Problem schematic for fixed/free $\langle 100 \rangle$ silicon nanowire with $\{100\}$ transverse surfaces.

$$\frac{\partial \Pi}{\partial \mathbf{u}_I} = \int_{\Omega_0^{bulk}} \mathbf{B}^{\mathrm{T}}\mathbf{S}\mathbf{F}^{\mathrm{T}}\mathrm{d}\Omega + \int_{\Gamma_0} \mathbf{B}^{\mathrm{T}}\mathbf{S}^s\mathbf{F}^{\mathrm{T}}\mathrm{d}\Gamma - \int_{\Gamma_0} N_I\mathbf{T}\mathrm{d}\Gamma, \tag{35}$$

where $\mathbf{S}$ is the PK2 stress due to the bulk strain energy, $\mathbf{S}^s$ is the surface PK2 stress defined in (30) and $\mathbf{B}^{\mathrm{T}}$ represents the derivative of the strain with respect to $\mathbf{u}_I$.

What has been accomplished in (35) is a systematic manner of obtaining continuum stress measures by calculating the system potential energy as a function of bulk and surface components. By correctly calculating the system energy, standard continuum mechanics relationships can
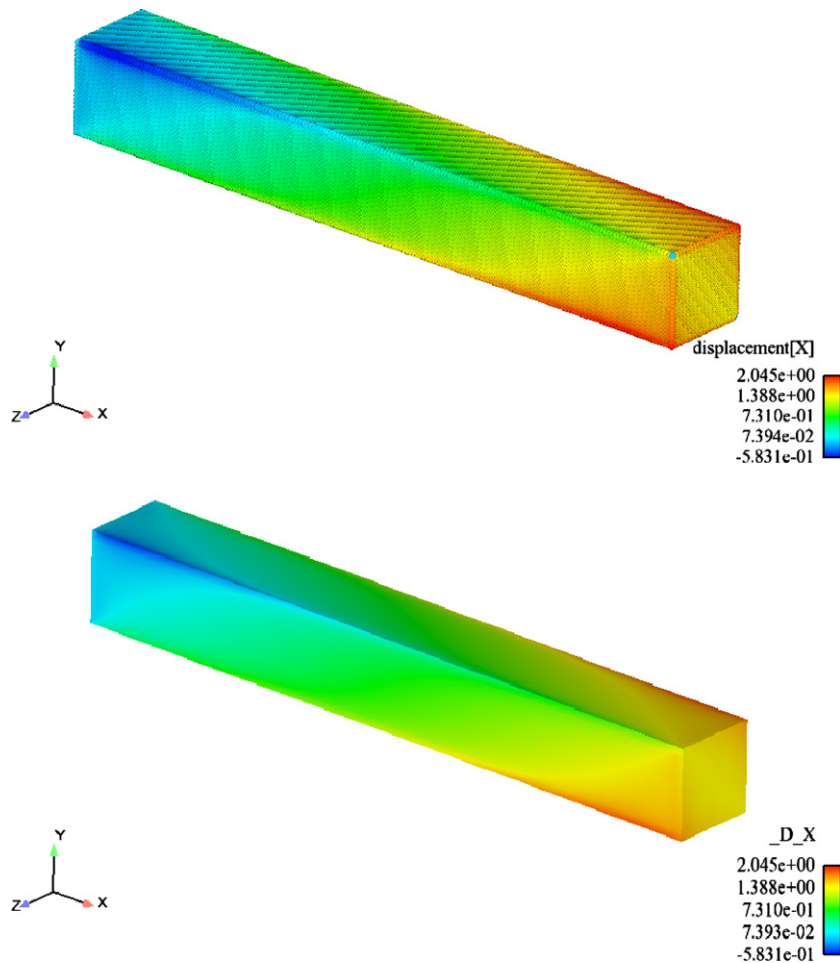

Fig. 4. Comparison between the calculated x-displacements using a (top) MS simulation and (bottom) SCB simulation of a fixed/free silicon nanowire.

be utilized to derive stress measures for usage in FE computations. The salient feature of Eq. (35) is that as the surface area to volume ratio becomes larger, the surface area terms will dominate the energetic expression. Because the stresses required for the FE internal forces are calculated by differentiating the strain energy density, correctly accounting for the surface energy will naturally lead to the correct forces on surface nodes. In contrast, if the volume of the bulk material is significantly larger than the surface area, then the potential energy from the surface terms will be insignificant compared to the volumetric potential energy, and the material will feel no effect from the surface stresses. Thus, this model degenerates to a BCB model as the length scale of the material increases.

5. 3D Numerical example: fixed/free silicon nanowire

We perform a 3D numerical example to test the performance of the SCB model for Tersoff-based silicon, using the T3 parameters given earlier in this work. The numerical example consists of a fixed/free silicon nanowire axially oriented in the $\langle 100 \rangle$ direction with unreconstructed $\{100\}$ transverse surfaces that had initial dimensions of $h = 95.6$ nm, while the cross sectional length $a = 11.9$ nm. As

seen in the problem schematic in Fig. 3, the nanowire was fixed at the $-x$ edge, while the $+x$ edge was free. No external forces were applied to the nanowire, such that all observed deformation occurs purely because of surface stresses, and no periodic boundary conditions were applied on any of the free surfaces.

A fully atomistic, molecular statics (MS) calculation was performed using the Sandia-developed simulation code LAMMPS [87] using the Tersoff potential and the Tersoff T3 parameters for comparison, while the SCB calculations were performed using the Sandia-developed simulation code Tahoe [88]. The MS calculation consisted of 698149 atoms, or nearly 2.1 million degrees of freedom. In comparison, the SCB model consisted of 8000 regularly spaced 8-node hexahedral elements, resulting in 9800 nodes and about 29,000 degrees of freedom. Both the MS and SCB calculations were performed quasistatically, with the goal being to compare the equilibrated minimum energy configurations due to the surface stresses.

A snapshot of the resulting minimum energy configurations for the MS and SCB calculations is shown in Fig. 4, which shows the axial (x)-displacements. In comparing the SCB and MS results, the SCB results capture most major features of the displacement field seen in the MS calcula-
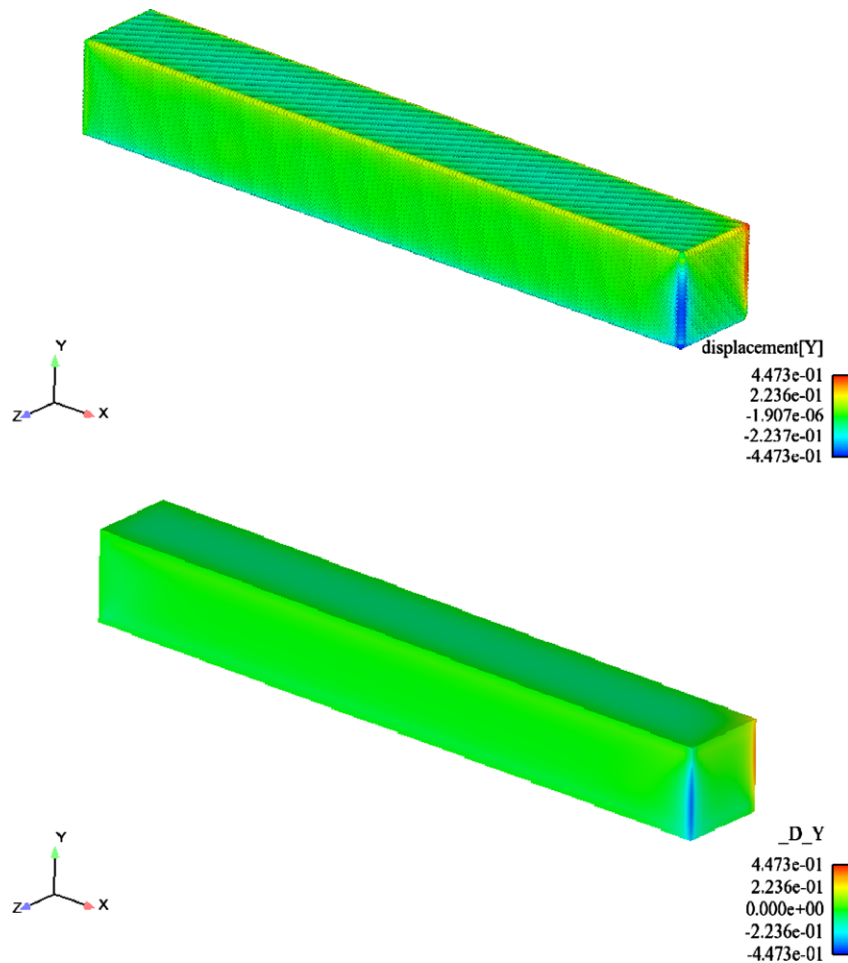

Fig. 5. Comparison between the calculated y-displacements using a (top) MS simulation and (bottom) SCB simulation of a fixed/free silicon nanowire.

tion. First of all, unlike the behavior observed in FCC metals [14–16], the silicon nanowires are predicted to expand rather than contract due to the surface stresses; the expansion is faithfully captured by the SCB calculation, and agree qualitatively with recent first-principles calculations for ultrasmall (<2 nm diameter) {100} silicon nanowires [24]. The expansion indicates that the surface stresses acting on the {100} surfaces as predicted by the T3 Tersoff potential are compressive, indicating that the surface is required to expand in order to reach a minimum energy configuration. Note that if the T2 parameters for the Tersoff potential are used, then essentially no surface relaxation due to surface stresses is predicted, in agreement with the predictions by Balamane et al. [78].

Interestingly, the MS results in Fig. 4 indicate that the expansion along the nanowire length due to the surface stresses is not homogeneous; this is likely due to asymmetry of the Tersoff potential at free surfaces in conjunction with the non-centrosymmetric DC lattice. Importantly, the SCB model captures these effects as observed in Fig. 4, indicating the ability to capture these critical surface-stress-driven effects.

We also compare the displacements at the center of the $+x$ face $(+x, 0, 0)$ for both the MS and SCB calculations. The MS displacement predicted an expansion of 1.43 Å, while the FEM nodal displacement using the SCB model predicted an expansion of 1.41 Å, indicating excellent agreement between the SCB model and the benchmark MS calculations.

It is important to mention here that the displacement of the surface FE nodes can be viewed as a combination of the FEM nodal displacement and the additional displacement due to the surface internal degrees of freedom Ξ^s given in Eq. (28), as the surface atoms in the surface unit cell depicted in Fig. 2 have a contribution to their total displacement due to Ξ^s. The surface internal degrees of freedom Ξ^s offer a correction of -0.0416 Å in this case, leading to a "total" displacement at $(+x, 0, 0)$ of 1.37 Å. This correction is insignificant relative to the overall length of the nanowire, but is important when compared to the unit cell dimensions, where the correction is nearly 1% of the silicon lattice parameter $a_0 = 5.432$ Å, and is about 1.5% of the interlayer spacing at the surface. We note that the surface expansion corresponds to a global tensile strain
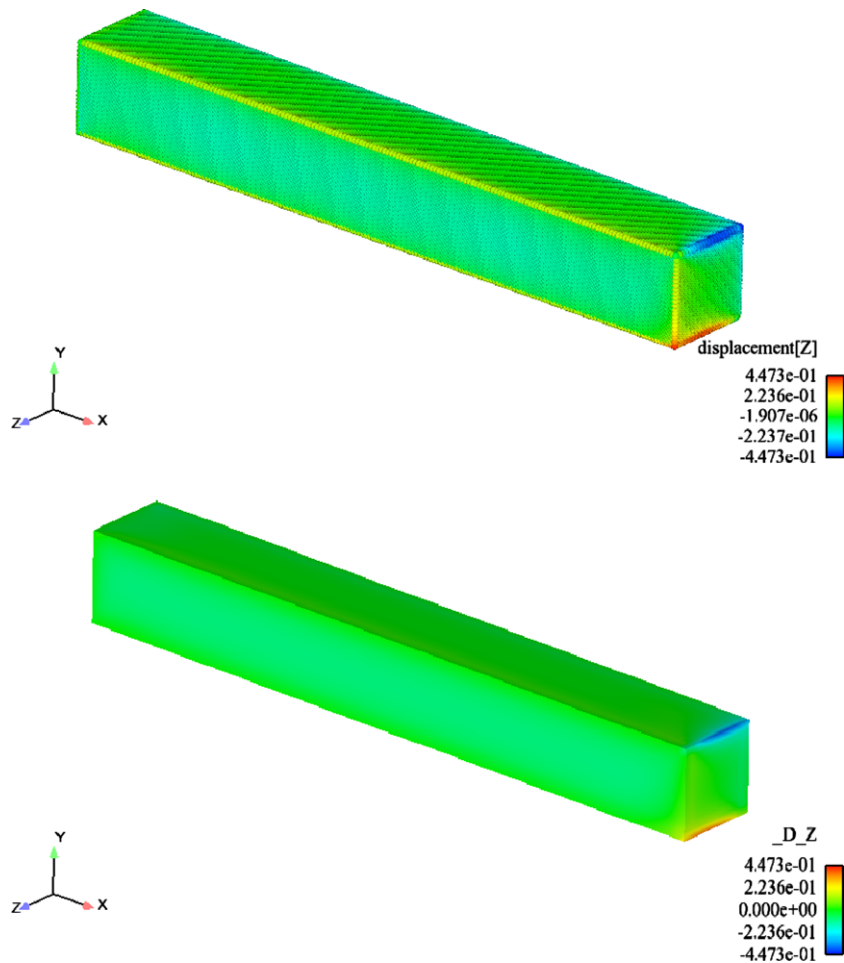

Fig. 6. Comparison between the calculated z-displacements using a (top) MS simulation and (bottom) SCB simulation of a fixed/free silicon nanowire.

of about 0.15%, which is smaller than that predicted in FCC metal nanowires [66].

The y and z displacements of the nanowire are shown in Figs. 5 and 6. The overall trends are captured accurately by the SCB model, including the correct positive and negative displacements of edges and corners. The accuracy of the SCB model deteriorates slightly at the edges and corners; this is likely because edge and corner atoms are not included in the surface unit cell, and thus the nodal deformation that is observed in these images is due to an average deformation of the elements connected to the edge or corner. However, note that the SCB model does correctly capture the contraction observed in both the $+/-$ y and z faces; this represents the capturing of the Poisson effect due to the overall expansion of the nanowire in the axial direction.

Regarding the contraction of the $+/-$ y and z faces due to the axial expansion, we compare the y displacements at the center of the $+y$ face $(+x/2, y/2, 0)$ between the MS and SCB calculations. The MS simulation predicted a contraction of about -0.133Å. The FEM nodal displacement was -0.091 Å. However, the surface internal degree of freedom at that point $\Xi^s = -0.044$ Å, leading to a "total" displacement of -0.135 Å, which is in very close agreement with the MS solution. Again, the correction of the internal degree of freedom is nearly 1% of the silicon lattice parameter a_0, and more than 1.5% of the interlayer spacing at the surface. An identical "total" solution is obtained on the $+z$ face $(+x/2, 0, +z/2)$, with identical accuracy to the full MS result.

Finally, we note that if a traditional BCB model is used that does not account for free surface effects, then zero relaxation would be observed.

6. Conclusions

In conclusion, we have formulated an extension to previously developed bulk Cauchy-Born models for diamond cubic lattice structures to capture surface stress effects due to the ideal, unreconstructed {100} surfaces of diamond cubic lattice structures. The diamond cubic lattice structure is an important one, as many semiconductors of interest such as silicon, germanium and their alloys form in this lattice structure. The major theoretical development as compared to previously developed bulk Cauchy-Born models for silicon is an enlarged surface unit cell that captures: (1) The effects of undercoordinated surface atoms and surface bonding, which lead naturally to the existence of surface stresses, (2) The noncentrosymmetric nature of the diamond cubic lattice, and (3) The relaxation of interpenetrating FCC lattices at free surfaces through the addition of appropriate internal surface degrees of freedom.

The Surface Cauchy-Born model for diamond cubic lattices was tested through comparison with fully atomistic calculations of the minimum energy configurations of fixed/free silicon nanowires modeled using the Tersoff

potential. The Surface Cauchy-Born model was shown to capture the major features of the deformation induced by surface stresses at a significantly reduced computational cost, particularly in the expansion of the free end of the nanowire due to the compressive surface stresses, and the inhomogeneity of the tensile deformation resulting from the surface stresses.

Future work will focus on developing SCB representations for both dimerized 2×1 {100} surfaces, as well as passivated {100} surfaces.

References

[1] C.M. Lieber, Nanoscale science and technology: building a big future from small things, MRS Bull. 28 (7) (2003) 486–491.
[2] P. Yang, The chemistry and physics of semiconductor nanowires, MRS Bull. 30 (2) (2005) 85–91.
[3] Y. Xia, P. Yang, Y. Sun, Y. Wu, B. Mayers, B. Gates, Y. Yin, F. Kim, H. Yan, One-dimensional nanostructures: synthesis, characterization, and applications, Adv. Mater. 15 (5) (2003) 353–389.
[4] H.G. Craighead, Nanoelectromechanical systems, Science 290 (2000) 1532–1535.
[5] N.V. Lavrik, M.J. Sepaniak, P.G. Datskos, Cantilever transducers as a platform for chemical and biological sensors, Rev. Sci. Instrum. 75 (7) (2004) 2229–2253.
[6] K.L. Ekinci, Electromechanical transducers at the nanoscale: actuation and sensing of motion in nanoelectromechanical systems (NEMS), Small 1 (8–9) (2005) 786–797.
[7] Y. Cui, Q. Wei, H. Park, C.M. Lieber, Nanowire nanosensors for highly sensitive and selective detection of biological and chemical species, Science 293 (2001) 1289–1292.
[8] G.T. Reed, Device physics – the optical age of silicon, Nature 427 (2004) 595–596.
[9] L.T. Canham, Silicon quantum wire array fabricated by electrochemical and chemical dissolution of wafers, Appl. Phys. Lett. 57 (10) (1990) 1046–1048.
[10] S.S. Verbridge, D.F. Shapiro, H.G. Craighead, J.M. Parpia, Macroscopic tuning of nanomechanics: substrate bending for reversible control of frequency and quality factor of nanostring resonators, Nano Letters 7 (6) (2007) 1728–1735.
[11] A.N. Cleland, M.L. Roukes, Fabrication of high frequency nanometer scale mechanical resonators from bulk Si crystals, Appl. Phys. Lett. 69 (18) (1996) 2653–2655.
[12] R.C. Cammarata, Surface and interface stress effects in thin films, Prog. Surf. Sci. 46 (1) (1994) 1–38.
[13] W. Haiss, Surface stress of clean and adsorbate-covered solids, Rep. Progr. Phys. 64 (2001) 591–648.
[14] J. Diao, K. Gall, M.L. Dunn, Surface-stress-induced phase transformation in metal nanowires, Nature Mater. 2 (10) (2003) 656–660.
[15] H.S. Park, K. Gall, J.A. Zimmerman, Shape memory and pseudoelasticity in metal nanowires, Phys. Rev. Lett. 95 (2005) 255504.
[16] W. Liang, M. Zhou, F. Ke, Shape memory effect in Cu nanowires, Nano Letters 5 (10) (2005) 2039–2043.
[17] D.W. Carr, S. Evoy, L. Sekaric, H.G. Craighead, J.M. Parpia, Measurement of mechanical resonance and losses in nanometer scale silicon wires, Appl. Phys. Lett. 75 (7) (1999) 920–922.
[18] T.D. Stowe, K. Yasumura, T.W. Kenny, D. Botkin, K. Wago, D. Rugar, Attonewton force detection using ultrathin silicon cantilevers, Appl. Phys. Lett. 71 (2) (1997) 288–290.

[19] J. Yang, T. Ono, M. Esashi, Surface effects and high quality factors in ultrathin single-crystal silicon cantilevers, Appl. Phys. Lett. 77 (23) (2000) 3860–3862.

[20] X. Li, T. Ono, Y. Wang, M. Esashi, Ultrathin single-crystalline-silicon cantilever resonators: fabrication technology and significant specimen size effect on Young's modulus, Appl. Phys. Lett. 83 (15) (2003) 3081–3083.

[21] J. Yang, T. Ono, M. Esashi, Investigating surface stress: surface loss in ultrathin single-crystal silicon cantilevers, J. Vacuum Sci. Tech. B 19 (2) (2001) 551–556.

[22] J. Yang, T. Ono, M. Esashi, Mechanical behavior of ultrathin microcantilevers, Sensor Actuator 82 (2000) 102–107.

[23] J.Q. Broughton, C.A. Meli, P. Vashishta, R.K. Kalia, Direct atomistic simulation of quartz crystal oscillators: bulk properties and nanoscale devices, Phys. Rev. B 56 (2) (1997) 611–618.

[24] B. Lee, R.E. Rudd, First-principles calculation of mechanical properties of Si ⟨100⟩ nanowires and comparison to nanomechanical theory, Phys. Rev. B 75 (2007) 195328.

[25] E.W. Wong, P.E. Sheehan, C.M. Lieber, Nanobeam mechanics: elasticity, strength, and toughness of nanorods and nanotubes, Science 277 (1997) 1971–1975.

[26] S. Cuenot, C. Frétigny, S. Demoustier-Champagne, B. Nysten, Surface tension effect on the mechanical properties of nanomaterials measured by atomic force microscopy, Phys. Rev. B 69 (2004) 165410.

[27] B. Wu, A. Heidelberg, J.J. Boland, Mechanical properties of ultrahigh-strength gold nanowires, Nature Mater. 4 (2005) 525–529.

[28] G.Y. Jing, H.L. Duan, X.M. Sun, Z.S. Zhang, J. Xu, Y.D. Li, J.X. Wang, D.P. Yu, Surface effects on elastic properties of silver nanowires: contact atomic-force microscopy, Phys. Rev. B 73 (2006) 235409.

[29] L.G. Zhou, H. Huang, Are surfaces elastically softer or stiffer? Appl. Phys. Lett. 84 (11) (2004) 1940–1942.

[30] V.B. Shenoy, Atomistic calculations of elastic properties of metallic FCC crystal surfaces, Phys. Rev. B 71 (2005) 094104.

[31] H. Liang, M. Upmanyu, H. Huang, Size-dependent elasticity of nanowires: nonlinear effects, Phys. Rev. B 71 (2005) 241403(R).

[32] C. Ji, H.S. Park, Characterizing the elasticity of hollow metal nanowires, Nanotechnology 18 (2007) 115707.

[33] H.S. Park, J.A. Zimmerman, Modeling inelasticity and failure in gold nanowires, Phys. Rev. B 72 (2005) 054106.

[34] H.S. Park, K. Gall, J.A. Zimmerman, Deformation of FCC nanowires by twinning and slip, J. Mech. Phys. Solids 54 (9) (2006) 1862–1881.

[35] A.F. Voter, F. Montalenti, T.C. Germann, Extending the time scale in atomistic simulation of materials, Annu. Rev. Mater. Res. 32 (2002) 321–346.

[36] M.E. Gurtin, A. Murdoch, A continuum theory of elastic material surfaces, Arch. Ration. Mech. Anal. 57 (1975) 291–323.

[37] F.H. Streitz, R.C. Cammarata, K. Sieradzki, Surface-stress effects on elastic properties I. Thin metal films, Phys. Rev. B 49 (15) (1994) 10699–10706.

[38] R.E. Miller, V.B. Shenoy, Size-dependent elastic properties of nanosized structural elements, Nanotechnology 11 (2000) 139–147.

[39] D.E. Segall, S. Ismail-Beigi, T.A. Arias, Elasticity of nanometer-sized objects, Phys. Rev. B 65 (2002) 214109.

[40] L.H. He, C.W. Lim, B.S. Wu, A continuum model for size-dependent deformation of elastic films of nano-scale thickness, Int. J. Solids Struct. 41 (2004) 847–857.

[41] P. Sharma, S. Ganti, N. Bhate, Effect of surfaces on the size-dependent elastic state of nano-inhomogeneities, Appl. Phys. Lett. 82 (4) (2003) 535–537.

[42] C.T. Sun, H. Zhang, Size-dependent elastic moduli of platelike nanomaterials, J. Appl. Phys. 92 (2) (2003) 1212–1218.

[43] R. Dingreville, J. Qu, M. Cherkaoui, Surface free energy and its effect on the elastic behavior of nano-sized particles, wires and films, J. Mech. Phys. Solids 53 (2005) 1827–1854.

[44] G. Wei, Y. Shouwen, H. Ganyun, Finite element characterization of the size-dependent mechanical behaviour in nanosystems, Nanotechnology 17 (2006) 1118–1122.

[45] J. Wang, H.L. Duan, Z.P. Huang, B.L. Karihaloo, A scaling law for properties of nano-structured materials, Proc. Royal Soc. A 462 (2006) 1355–1363.

[46] P. Lu, H.P. Lee, C. Lu, S.J. O'Shea, Surface stress effects on the resonance properties of cantilever sensors, Phys. Rev. B 72 (2005) 085405.

[47] M.E. Gurtin, X. Markenscoff, R.N. Thurston, Effects of surface stress on the natural frequency of thin crystals, Appl. Phys. Lett. 29 (9) (1976) 529–530.

[48] J.E. Sader, Surface stress induced deflections of cantilever plates with applications to the atomic force microscope: rectangular plates, J. Appl. Phys. 89 (5) (2001) 2911–2921.

[49] A.W. McFarland, M.A. Poggi, M.J. Doyle, L.A. Bottomley, J.S. Colton, Influence of surface stress on the resonance behavior of microcantilevers, Appl. Phys. Lett. 87 (2005) 053505.

[50] E. Tadmor, M. Ortiz, R. Phillips, Quasicontinuum analysis of defects in solids, Philos. Magn. A 73 (1996) 1529–1563.

[51] L.E. Shilkrot, R.E. Miller, W.A. Curtin, Multiscale plasticity modeling: coupled atomistics and discrete dislocation mechanics, J. Mech. Phys. Solids 52 (2004) 755–787.

[52] J. Fish, W. Chen, Discrete-to-continuum bridging based on multigrid principles, Comput. Meth. Appl. Mech. Engrg. 193 (2004) 1693–1711.

[53] P.A. Klein, J.A. Zimmerman, Coupled atomistic-continuum simulation using arbitrary overlapping domains, J. Comput. Phys. 213 (2006) 86–116.

[54] F.F. Abraham, J. Broughton, N. Bernstein, E. Kaxiras, Spanning the continuum to quantum length scales in a dynamic simulation of brittle fracture, Europhys. Lett. 44 (1998) 783–787.

[55] R.E. Rudd, J.Q. Broughton, Coarse-grained molecular dynamics and the atomic limit of finite elements, Phys. Rev. B 58 (1998) 5893–5896.

[56] W. E, Z.Y. Huang, A dynamic atomistic-continuum method for the simulation of crystalline materials, J. Comput. Phys. 182 (2002) 234–261.

[57] G.J. Wagner, W.K. Liu, Coupling of atomistic and continuum simulations using a bridging scale decomposition, J. Comput. Phys. 190 (2003) 249–274.

[58] H.S. Park, E.G. Karpov, W.K. Liu, P.A. Klein, The bridging scale for two-dimensional atomistic/continuum coupling, Philos. Magn. 85 (1) (2005) 79–113.

[59] H.S. Park, E.G. Karpov, W.K. Liu, A temperature equation for coupled atomistic/continuum simulations, Comput. Meth. Appl. Mech. Engrg. 193 (2004) 1713–1732.

[60] S.P. Xiao, T. Belytschko, A bridging domain method for coupling continua with molecular dynamics, Comput. Meth. Appl. Mech. Engrg. 193 (2004) 1645–1669.

[61] W.K. Liu, E.G. Karpov, H.S. Park, Nano Mechanics and Materials: Theory, Multiscale Methods and Applications, John Wiley and Sons, 2006.

[62] X. Li, W. E, Multiscale modeling of the dynamics of solids at finite temperature, J. Mech. Phys. Solids 53 (2005) 1650–1685.

[63] W.K. Liu, E.G. Karpov, S. Zhang, H.S. Park, An introduction to computational nano mechanics and materials, Comput. Meth. Appl. Mech. Engrg. 193 (2004) 1529–1578.

[64] W.A. Curtin, R.E. Miller, Atomistic/continuum coupling in computational materials science, Model. Simul. Mater. Sci. Engrg. 11 (2003) R33–R68.

[65] H.S. Park, P.A. Klein, G.J. Wagner, A Surface Cauchy-Born model for nanoscale materials, Int. J. Numer. Meth. Engrg. 68 (2006) 1072–1095.

[66] H.S. Park, P.A. Klein, Surface cauchy-born analysis of surface stress effects on metallic nanowires, Phys. Rev. B 75 (2007) 085408.

[67] H.S. Park, P.A. Klein, Boundary condition and surface stress effects on the resonant properties of metal nanowires, J. Mech. Phys. Solids, submitted for publication.

[68] M. Born, On the stability of crystals, i, Proc. Cambridge Philos. Soc. 36 (1940) 160–172.

[69] I. Stakgold, The Cauchy relations in a molecular theory of elasticity, Quart. Appl. Mech. 8 (1950) 169–186.

[70] J.H. Weiner, Hellman-Feynman theorem, elastic moduli, and the Cauchy relation, Phys. Rev. B 24 (1981) 845–848.

[71] G. Yun, H.S. Park, Surface cauchy-born modeling of nanoscale resonant mass sensing, Comput. Meth. Appl. Mech. Engrg., submitted for publication.

[72] G. Yun, H.S. Park, A multiscale, finite deformation formulation for surface stress effects on the coupled thermomechanical behavior of nanomaterials, Comput. Meth. Appl. Mech. Engrg., submitted for publication.

[73] E.B. Tadmor, G.S. Smith, N. Bernstein, E. Kaxiras, Mixed finite element and atomistic formulation for complex crystals, Phys. Rev. B 59 (1) (1999) 235–245.

[74] J. Tersoff, New empirical approach for the structure and energy of covalent systems, Phys. Rev. B 37 (12) (1988) 6991–7000.

[75] J. Tersoff, Modeling solid-state chemistry: interatomic potentials for multicomponent systems, Phys. Rev. B 39 (8) (1989) 5566–5568.

[76] Z. Tang, H. Zhao, G. Li, N.R. Aluru, Finite-temperature quasicontinuum method for multiscale analysis of silicon nanostructures, Phys. Rev. B 74 (2006) 064110.

[77] H. Zhao, Z. Tang, G. Li, N.R. Aluru, Quasiharmonic models for the calculation of thermodynamic properties of crystalline silicon under strain, J. Appl. Phys. 99 (2006) 064314.

[78] H. Balamane, T. Halicioglu, W.A. Tiller, Comparative study of silicon empirical interatomic potentials, Phys. Rev. B 46 (4) (1992) 2250–2279.

[79] A. Ramstad, G. Brocks, P.J. Kelly, Theoretical study of the Si (100) surface reconstruction, Phys. Rev. B 51 (20) (1995) 14504–14523.

[80] M. Arroyo, T. Belytschko, An atomistic-based finite deformation membrane for single layer crystalline films, J. Mech. Phys. Solids 50 (2002) 1941–1977.

[81] P. Zhang, Y. Huang, P.H. Geubelle, P.A. Klein, K.C. Hwang, The elastic modulus of single-wall carbon nanotubes: a continuum analysis incorporating interatomic potentials, Int. J. Solids Struct. 39 (2002) 3893–3906.

[82] T. Belytschko, W.K. Liu, B. Moran, Nonlinear Finite Elements for Continua and Structures, John Wiley and Sons, 2002.

[83] P.A. Klein, A virtual internal bond approach to modeling crack nucleation and growth, Ph.D. Thesis (1999) Stanford University.

[84] M.S. Daw, M.I. Baskes, Embedded-atom method: derivation and application to impurities, surfaces, and other defects in metals, Phys. Rev. B 29 (12) (1984) 6443–6453.

[85] J. Tersoff, Empirical interatomic potential for silicon with improved elastic properties, Phys. Rev. B 38 (14) (1988) 9902–9905.

[86] T.J.R. Hughes, The Finite Element Method: Linear Static and Dynamic Finite Element Analysis, Prentice-Hall, 1987.

[87] Warp, http://www.cs.sandia.gov/~sjplimp/lammps.html.

[88] Tahoe, http://tahoe.ca.sandia.gov.